International Journal of Automotive Technology, Vol. 19, No. 3, pp. 443−453 (2018)
DOI 10.1007/s12239−018−0043−y

pISSN 1229−9138/ eISSN 1976−3832

LOAD AND LOAD DEPENDENT FRICTION IDENTIFICATION AND COMPENSATION OF ELECTRONIC NON-CIRCULAR GEAR BRAKE SYSTEM

Heeram Park and Seibum Choi*

Department of Mechanical Engineering, KAIST, Daejeon 34141, Korea

(Received 16 November 2016; Revised 5 April 2017; Accepted 31 May 2017)

ABSTRACT−Control of the electronic non-circular gear brake (ENGB) involves challenges, including the non-linear variation of loads and the effect of friction, which is dependent upon load. The controller must be designed based on modelling information in order to enhance control performance. This study performed model identification of the ENGB system using a DOB-based model identification method. By employing the nearest neighbor search method, the even-odd disturbance was separated without the influence of hysteresis even in situations with low control precision. The accuracy of the resulting ENGB system model was validated through experiments. The self-energizing effect due to friction between the brake disc and pad within the mechanical system was also validated.

KEY WORDS : Load dependent friction, Friction model identification, EMB, Electronic non-circular gear brake

1. INTRODUCTION

With the growing social interest in automobile safety and environmental issues, the development of environment-friendly and intelligent vehicles is increasingly popular, resulting in the vigorous development of related technologies. Against this backdrop, brake-by-wire technology has emerged as the braking option most suitable to consumer demand, and is consistent with the technological development trends of the current automobile industry.

Brake-by-wire technology physically separates the driver from the brake by transmitting the driver's intent to brake to an electronic control unit (ECU) not through a mechanical connection device, but using electric signals. The braking power is then controlled by the operation of a hydrodynamic or electronic actuator. The types of electronic actuator used for this purpose are specifically divided into two categories, the general method (electromechanical brake) and a method of amplifying power with a wedge (electronic wedge brake). Developed by Siemens VDO, the electrical wedge brake system achieves the highest energy efficiency among the brake-by-wire systems by using a self-reinforcement effect, based on the structural characteristics of the wedge-shaped members (Hartmann *et al.*, 2002).

Control of the electromechanical brake (EMB) or electronic wedge brake (EWB) involves challenges, including the non-linear variation of loads and the effect of friction, which is dependent upon load. Previously the EMB and EWB were controlled by a controller based on the proportional-integral (PI) cascaded control (Robert *et al.*, 2004; Balogh *et al.*, 2007; Fox *et al.*, 2007; Kim *et al.*, 2009a; Semsey and Roberts, 2006; Xiang *et al.*, 2008). Depending on the reaction speed of the subsystem, the current control loop is located in the innermost position, while the outer side has the loop controlling clamping force or position. Because of the wide variation in load and the non-linear characteristics of the brake system, a PI cascaded controller using a fixed gain cannot produce constant performance within varying operating ranges.

The controller must be designed based on modelling information in order to enhance control performance. Research has been conducted with controllers that are designed to make the P gain of the PI clamping force controller proportionate to the clamping force (Roberts *et al.*, 2003). Other studies have examined improvements in control performance based on a feedforward controller using a clamping force and friction model (Schwarz *et al.*, 1999; Saric *et al.*, 2008).

The toughest challenge in optimizing the EMB or EWB system is the fact that the clamping force and friction force are coupled with each other. In order to decouple them, a complicated reference trajectory and sampling techniques are being used.

Schwarz *et al.* (1999) and Saric *et al.* (2008) suggested a method of estimating clamping force using only the location of the motor and measurement of electric current, but without a clamping force sensor.

This study used an electronic non-circular gear brake

**Corresponding author.* e-mail: sbchoi@kaist.ac.kr

system, a type of EWB. Kim *et al.* (2008) developed a new self-energizing brake system that uses an oval gear called an electronic non-circular gear brake (ENGB). This brake system uses the oval gear and the self-reinforcement effect, as in the case of the EWB, but has the potential to be applied to a wider range of angles compared to the EWB, which only uses a certain angle.

However, because of the difficulty of producing an oval gear, instead of the oval gear of the original design, two older gears were laid together to form a new shape of gear. The first prototype of the ENGB had a large size, and its structure made it difficult to install within the wheel housing. In addition, a high load caused bending of the screw, which led to non-linear friction and deterioration of performance. This study used hardware that was modified from the prototype mentioned above.

Chapter 2 introduces the structure and actuation principles of the ENGB system and then performs the mathematical modeling of the ENGB system. Chapter 3 conducts model identification of the ENGB system, starting with the identification and compensation of the cogging torque of the PMSM. Chapter 4 and 5, the disturbance measured through the DOB was separated into torque generated by load and torque by coulomb friction, by using the even-odd decomposition method, and each is identified. Additionally, the identified models are verified through experiments. Lastly, Chapter 6 summarizes the research and discusses what needs to be studied further.

2. MATHEMATICAL MODEL OF ELECTRONIC NON-CIRCULAR GEAR BRAKE SYSTEM

Figure 1 demonstrates the modified ENGB system. The torque generated in the motor is transmitted to the ball-screw through a reduction gear. The rotary motion of the ball-screw is transformed into a rectilinear motion, and the screw nut operates the brake pad via a lever. The normal-direction displacement of the brake pad is determined by the non-circular gear.

2.1. ENGB Mechanical Part Dynamic Model

The dynamic equation of the ENGB mechanical part is expressed as follows.

$$T_{\mathrm{M}} = J\dot{\omega}(t) + B\omega(t) + T_{\mathrm{L}} + T_{\mathrm{C}} + T_{\mathrm{cog}} \tag{1}$$

Here, T_{M} refers to torque generated by the PMSM, $J\dot{\omega}(t)$ to the inertia moment of the ENGB system, $B\omega(t)$ to viscous friction torque, T_{L} to load torque generated by clamping force, T_{C} to coulomb friction, and T_{cog} to cogging torque. The load T_{L} created by clamping force was modeled based on the following assumption.

Assumption 1.
Since the sub-system from the reduction gear to the brake pad has significant speed with sufficiently high stiffness and sufficiently low inertia, therefore the dynamics of each

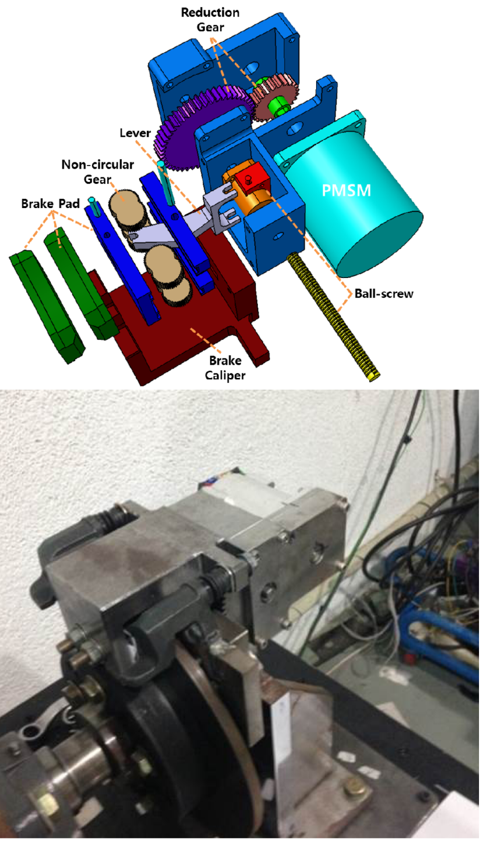

Figure 1. Structure and actual shape of the electronic non-circular gear brake.

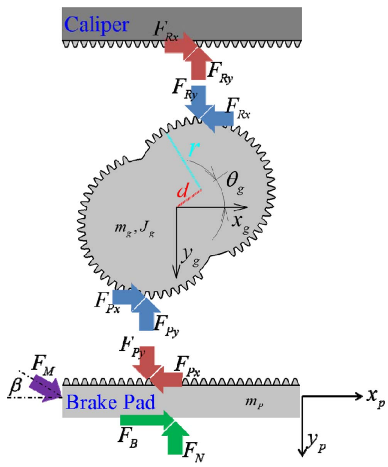

Figure 2. Free-body diagram of a non-circular gear and brake pad.

component within the 1 ~ 5 Hz brake system can be ignored.

The model of ENGB can be obtained by going back from the brake pad to the PMSM. Figure 2 shows the free body diagram of the brake pad and non-circular gear. Based on Assumption 1, the following force balance equation of the brake pad is obtained.

$$\sum F_x = F_M \cos\beta + F_B - F_{Px} = 0 \tag{2}$$

$$F_B = \mu F_N \tag{3}$$

$$\sum F_y = F_M \sin\beta + F_{Py} - F_N = 0 \tag{4}$$

Here, F_M refers to the force of the lever pushing the brake pad, F_B to the friction-caused braking force between the pad and disc, F_{Px} and F_{Py} to the parallel-direction and normal-direction reaction forces from the non-circular gear to the brake pad, μ to the friction factor of the brake pad, and F_N to the normal force from the brake disc to the brake pad.

Next, the following is the force balance equation of the non-circular gear.

$$\sum F_x = F_{Rx} - F_{Px} = 0 \tag{5}$$

$$\sum F_y = F_{Ry} - F_{Py} = 0 \tag{6}$$

$$\begin{aligned}\sum M_{gc} = (F_{Rx} + F_{Px})(r + d\sin\theta_g) \\ - (F_{Ry} + F_{Py}) d\cos\theta_g = 0\end{aligned} \tag{7}$$

Here, F_{Rx} and F_{Ry} refer to the parallel-direction and normal-direction reaction forces from the brake caliper to the non-circular gear, respectively, r to the diameter of one gear of the two overlapping gears, d to the distance from the center of the non-circular gear to the center of either gear, and θ_g to the rotation angle of the non-circular gear.

In Equation (7), the rotation angle θ_g of the non-circular gear has an operating range approaching zero, the values of $\sin\theta_g$ and $\cos\theta_g$ are approximated as 0 and 1, respectively. Based on Equations (5) ~ (7), the following equation is drawn.

$$F_{Px} = \frac{d}{r} F_{Py} \tag{8}$$

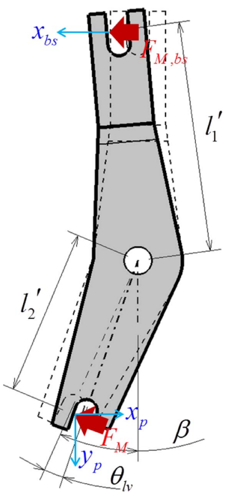

Figure 3. Free-body diagram of a lever actuator.

Applying Equations (2) ~ (4), the following equation is obtained for F_N and $F_{M,bs}$.

$$F_M = \frac{\mu - (d/r)}{\cos\beta + (d/r)\sin\beta} F_N \tag{9}$$

The load generated by clamping force is transferred to the ball screw nut via the lever. Figure 3 illustrates the free body diagram of the lever. The upper part of the lever is connected to the ball screw nut, while the bottom part is connected to the brake pad.

The relations between the force of the ball screw nut pushing the lever ($F_{m,bs}$) and the force pushing the lever and brake pad (F_m) are expressed as the torque balance equation for the center of rotation.

$$\begin{aligned} & l_1' F_{M,bs} \cos\theta_{lv} = l_2' F_M \\ & \left(l_1' = \frac{l_1}{\cos\theta_{lv}},\ l_2' = \frac{l_2\cos\beta + y_p}{\cos(\beta - \theta_{lv})} \right) \end{aligned} \tag{10}$$

Here, θ_{lv} refers to the lever's rotation angle, l_1' to the distance from the lever's center of rotation to the lever's point of contact with the ball screw nut, and l_2' to the distance from the lever's center of rotation to the lever's point of contact with the brake pad. Also, l_1 and l_2 refer to the distance when the lever's rotation angle is zero, and β to the lever's bent angle.

The force of the lever pushing the ball screw is converted into the torque rotating the ball screw bolt. This torque is then transferred to the PMSM via the reduction gear connected to the ball screw bolt. The relations between $F_{M,bs}$ and the torque (T_L) imposed upon the PMSM as a result of the clamping force is as follows.

$$T_L = \frac{L}{2\pi \cdot N_g \cdot \eta} F_{M,bs} \tag{11}$$

With Equations (9) and (10), T_L and F_N are expressed as the following.

$$\begin{aligned} & T_L = \frac{L \cdot l_2' \{\mu - (d/r)\}}{2\pi \cdot N_g \cdot \eta \cdot l_1' \{\cos\beta + (d/r)\sin\beta\}} F_N \\ & F_N = f(\theta) \end{aligned} \tag{12}$$

Friction torque T_C is expressed as in the following static coulomb friction model.

$$T_C = \begin{cases} (C_0 + C_1(F_N))\,\mathrm{sign}(\dot{\theta}_m) \\ \qquad \text{if } |\dot{\theta}_m| > \varepsilon \\ T_m - T_L \\ \qquad \text{if } |\dot{\theta}_m| < \varepsilon \text{ and } |T_m - T_L| < |T_{sf} + C_1(F_{cl})| \\ (T_{sf} + C_1(F_N))\,\mathrm{sign}(T_m - T_L) \quad \text{otherwise} \end{cases} \tag{13}$$

Here, C_0 refers to coulomb friction, C_1 to the constant dependent upon load, ε to the velocity near zero, and T_{sf} to static friction.

2.2. ENGB Kinematic Model Analysis

This section discusses the kinematics of the ENGB system, in the order of the PMSM, brake pad, and non-circular gear. Figure 4 demonstrates the reduction gear connecting the brake motor and ball screw. θ_M refers to the rotation angle of the helical gear (driving gear) directly connected to the PMSM, and θ_{bs} to the rotation angle of the gear (driven gear) directly connected to the ball screw. Meanwhile, r_1 refers to the diameter of the driving gear, while r_2 to that of the driven gear. The rotation angle of each gear can be expressed as the following.

$$\theta_{bs} = N_g \theta_M \quad \left(N_g = \frac{r_2}{r_1} \right) \tag{14}$$

Via the reduction gear, the power of the PMSM is transferred to the ball screw, where the rotation motion of the screw bolt is converted into the linear motion of the screw nut. The relations between the ball screw bolt's rotation angle (θ_{bs}) and the ball screw nut's balanced-direction displacement (x_{bs}) are expressed in the following equation.

$$x_{bs} = \frac{L}{2\pi} \theta_{bs} \tag{15}$$

The lever rotates around the central hinge. The upper part operates with the ball screw nut, while the bottom part is connected to the brake pad, generating the pad's displacement in the x direction (x_p). The relations between x_{bs} and the lever's rotation angle θ_{lv} are obtained as in the following equation.

$$x_{bs} = l_1' \sin\theta_{lv} = l_1 \tan\theta_{lv} \quad \left(l_1' = \frac{l_1}{\cos\theta_{lv}} \right) \tag{16}$$

Here, l_1 refers to the distance between the lever's rotation center at the initial position and the ball screw nut's point of contact, and l_1' refers to the distance after the lever's rotation. The relations between the lever's rotation angle θ_{lv} and the pad's parallel-direction displacement x_p are expressed as the following.

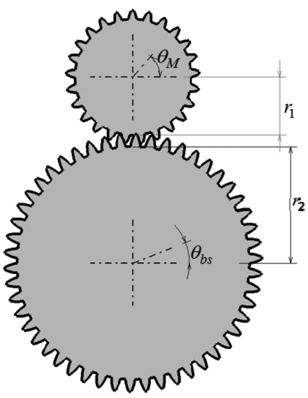

Figure 4. Reduction gear.

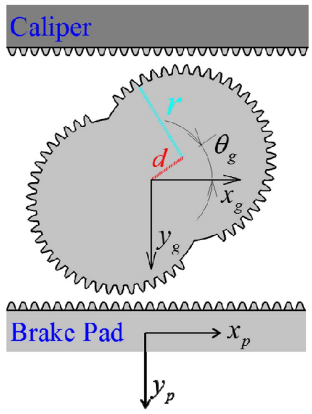

Figure 5. Non-circular gear.

$$x_p = l_2 \sin\beta - l_2' \cdot \sin(\beta - \theta_{lv}) \quad \left(l_2' = \frac{l_2 \cos\beta + y_p}{\cos(\beta - \theta_{lv})} \right) \tag{17}$$

$$x_p = l_2 \sin\beta - (l_2 \cos\beta + y_p) \cdot \tan(\beta - \theta_{lv}) \tag{18}$$

Here, β refers to the lever's bent angle, l_1 to the distance between the lever's rotation center at the initial position and the brake pad's point of contact, l_1' to the distance after the lever's rotation, and y_p to the normal-direction displacement of the brake pad. In addition, y_p is defined by the non-circular gear's rotation angle.

Figure 5 illustrates the two-dimensional movement of gear and pad. Here, x_p and y_p refer to the brake pad's parallel-direction and normal-direction displacement, x_g and y_g to the non-circular gear's parallel-direction and normal-direction displacement, θ_g to the gear's angle displacement, r to the non-circular gear's diameter, and d to half the distance between the center points of each circle of the non-circular gear. The relationship between the pad's parallel-direction and normal-direction displacement and the non-circular gear's angle displacement is expressed in the following Equation.

$$x_g = d(1 - \cos\theta_g) + r\theta_g \tag{19}$$

$$y_g = d\sin\theta_g \tag{20}$$

$$x_p = 2x_g \tag{21}$$

$$y_p = 2y_g \tag{22}$$

The above equations suggest that the non-circular gear's rotation angle and its normal-direction and parallel-direction displacement have non-linear relations. The system's high non-linearity makes it difficult to demonstrate dynamics, and calculation also becomes difficult because the controller uses complicated formulas. However, the actual actuation range of the ENGB system is within five degrees of the non-circular gear's rotation angle, and the non-linear terms of the sin and cos functions can be expressed as linear. In addition, $\sin\theta_g$ can be approximated as θ_g, and $\cos\theta_g$ as 1. Due to the significantly small error within the actuation range, the approximated values can be used instead. The above Equations (19) and (20) can be expressed with approximated values as in the following Equations (23) and (24).

$$x_g = r\theta_g \tag{23}$$

$$y_g = d\theta_g \tag{24}$$

3. IDENTIFICATION OF ENGB SYSTEM

3.1. Identification Method

The even-odd disturbance decomposition method was newly suggested by Dr. Gwang-hyeon Jo in 2013 as a means of identifying the ripple force and friction force of a permanent magnet linear synchronous motor. Due to the coupling of the cogging force and coulomb friction force, Dr. Jo proposed a method to separate them in an effort to solve the difficulty of trying to identify them together. By using the characteristics of cogging force, which is dependent on position, and friction force, which is dependent on velocity, the reference trajectory was adjusted to set position as an even function and velocity as an odd function in order to separate them. This research used the above method in order to separate load torque from friction torque. Since clamping force is dependent on position and friction torque depends on velocity, the same principle can be used to separate the two.

The above study used a high-performing actuator and driver and high-precision sensor to ensure precise control. The position tracking error was extremely small because position tracking was controlled without load, and therefore no compensation was required. However, the brake system used for this research had relatively poorer actuator, driver, and sensor performance. Since the position tracking error becomes unignorably high as a result of the clamping force and its friction dependence, relevant compensation was necessary. To settle this problem, the nearest neighbor search method was used. The entire identification process is as follows.

Step 0. Under symmetric reference trajectories.
Step 1. Position tracking control.
Step 2. Lumped disturbance estimation by a linear disturbance observer (DOB)
Step 3. Re-sampling obtained data using nearest neighbor search method
Step 4. Decomposition to even and odd disturbances from the estimated lumped disturbance.
Step 5. Load torque identification
Step 6. Friction torque identification.

3.2. Identification of ENGB System

In order to identify the non-linear model of the ENGB system, the identification of the linear nominal plant was first conducted. The linear part model of the ENGB system consists of torque constant, inertia, and viscous friction coefficient, as provided in the following.

$$T_M = J\dot{\omega}(t) + B\omega(t) \quad (T_M = K_T i_q) \tag{25}$$

As with the process of obtaining the PMSM's nominal model parameter, the step input test was implemented to obtain the ENGB system's nominal model parameter.

Figure 6 demonstrates the frequency response of the actual plant and model in bode plots. The experimental data is the velocity output data for a sine sweep signal input of 4 amps from 0 Hz to 10 Hz. Despite the existence of modeling error due to the non-linearity of cogging torque and friction torque, it is observed that the linear model is similar to the actual plant within the operating range of the ENGB. The linear model parameters of the ENGB system that were obtained as a result of experiments are provided in Table 1.

The identification of the non-linear disturbance was conducted according to the steps provided in Section 3.1.

Step 0. Reference trajectory

By making the motor move at a constant acceleration, data was configured to be evenly distributed across the entire

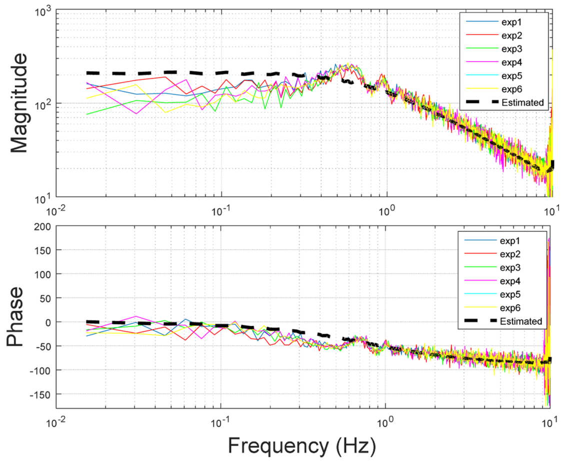

Figure 6. Bode plot of the frequency response obtained by various sine sweep input and the determined nominal model.

Table 1. ENGB system linear part parameters.

Parameter	Value (unit)
K_T	0.0174 (N·m/A)
J	6.813e-5 (Kg·m^2)
B	1.125e-3 (Kg·m^2/s)

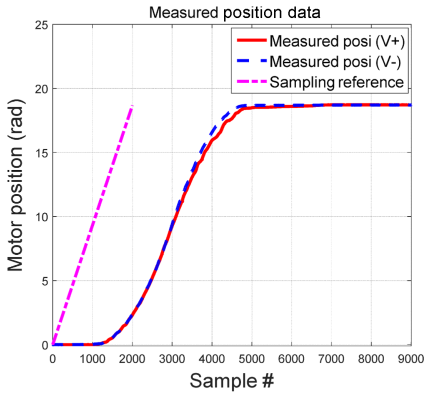

Figure 7. Measured data of the motor shown in the sample domain.

range of velocity domain. Also, the stop section was set so that the tracking error was converged to zero by the integral controller.

Step 1. Position tracking control

Using the nominal model and PID controller, the position tracking control of the above symmetric reference trajectory was conducted. The controller used can be expressed as the following equations.

$$u(t) = u_{\text{ff}}(t) + u_{\text{fb}}(t) \tag{26}$$

$$u_{\text{ff}}(t) = J\dot{\omega}_{\text{d}}(t) + B\omega_{\text{d}}(t) \tag{27}$$

$$u_{\text{fb}}(t) = K_{\text{d}}\dot{e}(t) + K_{\text{p}}e(t) + K_{\text{i}}\int_0^t e(\tau)d\tau \tag{28}$$

$$e(t) = \theta(t) - \theta_{\text{d}}(t) \tag{29}$$

Here, $u_{\text{ff}}(t)$ refers to the feedforward control input using the ENGB system's linear part model, $u_{\text{fb}}(t)$ to the PID feedback control input, $e(t)$ to the position tracking error, $\theta_{\text{d}}(t)$ to the reference position trajectory, and K_{p}, K_{i}, and K_{d} to the positive tuning parameters.

Step 2. Lumped disturbance estimation by a linear disturbance observer (DOB)

The result of estimating the lumped disturbance by using the DOB is provided in the following.

$$\hat{d}(t) = q(t) * \left[J\dot{\omega}(t) + B\omega(t) - u(t)\right] \tag{30}$$

Step 3. Re-sampling obtained data using nearest neighbor search method

Figure 7 indicates the motor position measured in the sample domain. The solid line refers to the data in case of clamping, and the dotted line to the reversed data, upon release. As a result, it is observed that position errors are generated in the sample of the same number. Using the nearest neighbor search method can make it possible to perform data analysis at the same position.

The nearest neighbor search method is an optimization method to find the data point nearest to a certain point among various data points. If the method is applied to one-dimensional data as in this research, a simple coding can be used for actuation.

$$\left[\theta_{\text{M}}(k)\right],\ \left[\theta_{\text{N}}(k)\right]\ k \in \text{N},\ 1 \le k \le N \tag{31}$$

$$\left[\theta_{\text{R}}(k)\right],\ j \in \text{N},\ 1 \le j \le M \qquad (M < N) \tag{32}$$

Here, $[\theta_{\text{M}}(k)]$ and $[\theta_{\text{N}}(k)]$ refer to the position data set in case of clamp and release, and $[\theta_{\text{R}}(j)]$ to the position data set that can be used as a comparative reference. In Figure 7, $[\theta_{\text{R}}(k)]$ is indicated as a chain line. The range of $[\theta_{\text{R}}(j)]$ is set to have the same position range as $[\theta_{\text{M}}(k)]$ and $[\theta_{\text{N}}(k)]$, as shown below.

$$\begin{aligned} \max\left[\theta_{\text{R}}(j)\right] &= \max\left[\theta_{\text{M}}(k)\right] = \max\left[\theta_{\text{N}}(k)\right] \\ \min\left[\theta_{\text{R}}(j)\right] &= \min\left[\theta_{\text{M}}(k)\right] = \min\left[\theta_{\text{N}}(k)\right] \end{aligned} \tag{33}$$

The nearest neighbor search method is expressed as the following.

$$\begin{aligned} J_1 &= \left\|\theta_{\text{R}}(j) - \theta_{\text{M}}(k)\right\|_2 \\ J_2 &= \left\|\theta_{\text{R}}(j) - \theta_{\text{N}}(k)\right\|_2 \end{aligned} \tag{34}$$

$$\left[\theta_{\text{R}M}(j,k')\right] = \left\{\theta_{\text{RM}} \in \theta_{\text{M}}, k' \in k \,\middle|\, \min(J_1)\right\} \tag{35}$$

$$\left[\theta_{\text{RN}}(j,k')\right] = \left\{\theta_{\text{RN}} \in \theta_{\text{N}}, k' \in k \,\middle|\, \min(J_2)\right\} \tag{36}$$

Here, $J_{1,2}$ refers to cost function, the distance between one data point of $[\theta_{\text{R}}(j)]$ and another data point of $[\theta_{\text{M}}(k)]$ and $[\theta_{\text{N}}(k)]$. In addition, $[\theta_{\text{RM}}(j, k')]$ and $[\theta_{\text{RN}}(j, k')]$ are the datasets minimizing each cost function and the sets of sample number.

If the lumped disturbance data is re-sampled by using the saved sample number, data calculation at the same position becomes possible. Figure 8 helps illustrate the nearest neighbor search method.

Figure 9 provides the results of re-sampling by applying the nearest neighbor search method to the data in Figure 7. It was observed that the position error of the sample number in case of clamping and release has been reduced to an ignorable level. Figure 10 shows the result of re-sampling the estimated lumped disturbance by using the saved sample number.

Step 4. Decomposition to even and odd disturbances from the estimated lumped disturbance.

Using the Equations (37) and (38), the disturbance can be divided as even and odd disturbances.

$$\left[\hat{d}(j)\right]_{\text{even}} = \frac{1}{2}\left[\hat{d}(j) + \hat{d}(M - j + 1)\right] \tag{37}$$

$$\left[\hat{d}(j)\right]_{\text{odd}} = \frac{1}{2}\left[\hat{d}(j) - \hat{d}(M - j + 1)\right] \tag{38}$$

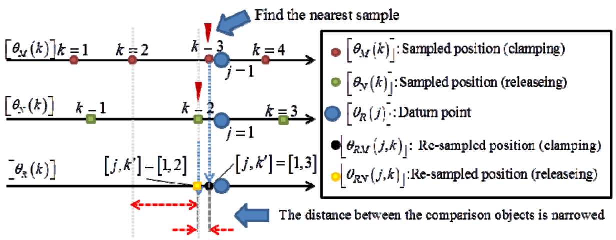

Figure 8. One dimensional nearest neighbor search method.

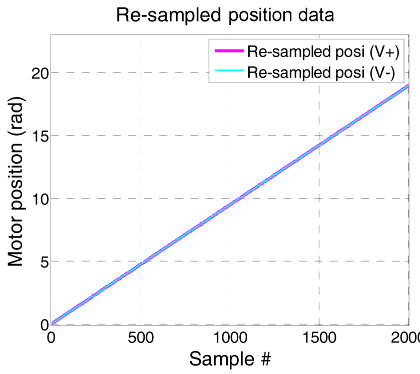

Figure 9. Re-sampled position data using nearest neighbor search method.

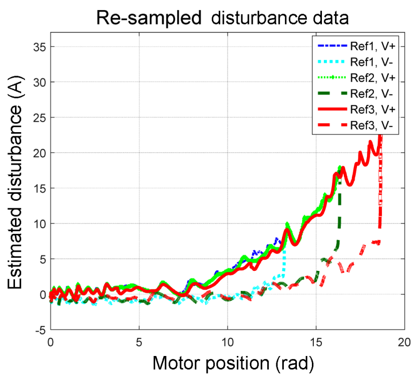

Figure 10. Re-sampled lumped disturbance.

When lumped disturbance (30) is divided using the above equation, even and odd disturbances can be expressed as follows.

$$\left[\hat{d}(j)\right]_{\text{even}} = \underbrace{-\left[T_L\left(\theta_R(j)\right)\right]_{\text{even}}}_{\text{dominant}} \underbrace{-\Delta J\dot{\omega}(j)}_{\text{negligible}} \underbrace{-\left[\hat{T}_{\mathrm{C}}\left(\theta_{\mathrm{R}}(j),\omega_{\mathrm{R}}(j)\right)\right]_{\text{even}}}_{\text{hysteresis effect of the friction force}} \quad (39)$$

$$\left[\hat{d}(j)\right]_{\text{odd}} = \underbrace{-\left[T_{\mathrm{C}}\left(\theta_{\mathrm{R}}(j),\omega_{\mathrm{R}}(j)\right)\right]_{\text{odd}}}_{\text{dominant}} \underbrace{-\Delta B\omega(j)}_{\text{negligible}} \quad (40)$$

The dominant component of the even disturbance is the

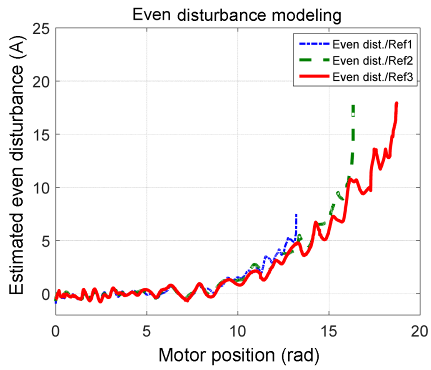

Figure 11. Even disturbance in position domain.

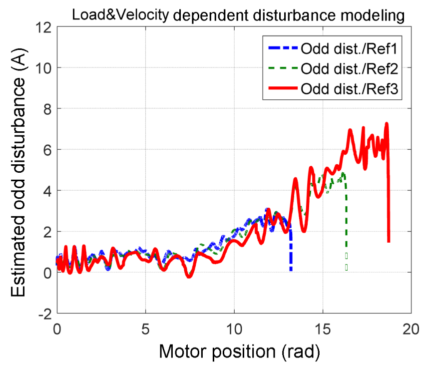

Figure 12. Odd disturbance in position domain.

torque produced by the load, while that of the odd disturbance is the coulomb friction. The remaining components, small enough to be negligible, are related to the parametric error of the linear model and the hysteresis of friction force. Figures 11 and 12 show the even disturbance and odd disturbance on the position domain.

Step 5. Load torque identification

Using the even disturbance data obtained in the previous step, the LS (least square) method can be applied to identify the load torque. A cubic equation was used to express the load torque. Equation (41) is the cost function that searches for the parameters of the cubic equation. The load torque approximated by the LS method is shown by the black dotted line in Figure 13. The identified load torque was similar to the previously obtained data.

$$\min_{\hat{p}_{n3},\hat{p}_{n2},\hat{p}_{n1},\hat{p}_{n0}} J = \sum_{j=1}^{M} \left[\begin{array}{l} -\left[\hat{d}\left(\theta_{\mathrm{R}}(j)\right)\right]_{\text{even}} \\ -\left[\begin{array}{l} \hat{p}_{n3}\cdot\theta_{\mathrm{R}}^{3}(j)+\hat{p}_{n2}\cdot\theta_{\mathrm{R}}^{3}(j) \\ +\hat{p}_{n1}\cdot\theta_{\mathrm{R}}^{3}(j)+\hat{p}_{n0} \end{array} \right] \end{array} \right] \quad (41)$$

Step 6. Friction torque identification

Figure 14 presents the odd disturbance in the load domain using the load torque obtained in Step 5. The graph shows

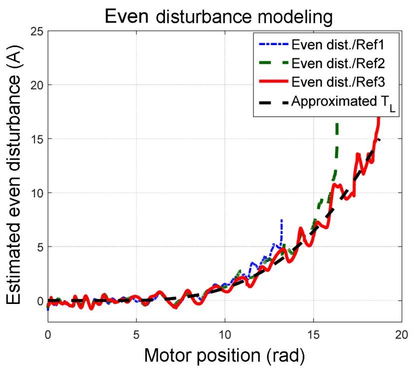

Figure 13. Approximated load torque.

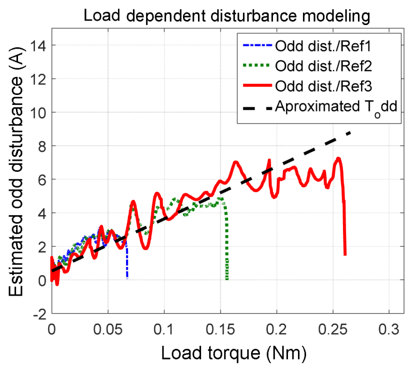

Figure 14. Approximated load dependent coulomb friction torque.

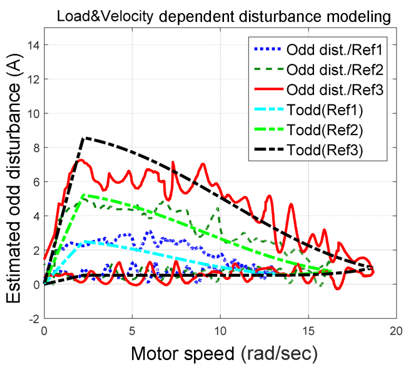

Figure 15. Approximated velocity dependent friction torque (speed domain).

that the odd disturbance is directly proportionate to the load, and that the friction increases. Similar to Step 5, the LS method was employed to approximate the load dependent friction torque. The black dotted line in Figure 14 represents the results approximated with the cost function of (42).

$$\min_{\hat{C}_1,\hat{C}_0} J = \sum_{j=1}^{M}\begin{bmatrix} -\left[\hat{d}\left(\theta_R(j)\right)\right]_{odd} \\ -\left[\left\{\hat{C}_0 + \hat{C}_1 \cdot \hat{T}_L\left(\theta_R(j)\right)\right\}\cdot \mathrm{sgn}\left(\omega_R(j)\right)\right] \end{bmatrix} \tag{42}$$

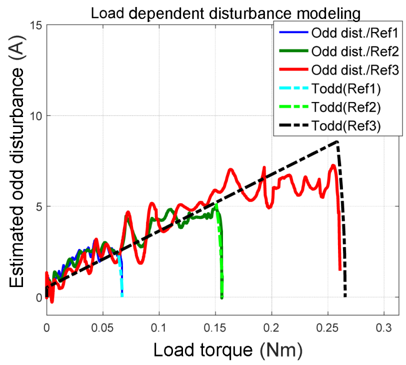

Figure 16. Approximated load and velocity dependent friction torque (load torque domain).

Nonlinearity is observed in Figure 14, which shows the end of the odd disturbance falls to 0. This is because friction torque is affected not only by load, but also velocity at low speeds. Figure 15 gives the odd disturbance in the speed domain.

The disturbance data obtained with the sensor, which exhibited unsatisfactory performance, were insufficient in expressing the actual friction torque. The friction torque at low speeds was approximated using the saturation function. The approximated model of the load dependent friction torque is represented by the dotted line in Figure 16, and we can see that the results are similar to the obtained data.

4. ENGB MODEL VALIDATION

The validation of the model obtained from experiments is described in this section. Three validation methods were used. The first method compared control precision for the identified model with and without a feed forward controller.

Figures 17 and 18 present the validation results obtained using the first method. The position tracking error in these Figures reveal a significant decrease in error for the identified model with the feed-forward controller compared to the model with only PID. Under high loads, the model with only PID had a maximum error and rms error of 0.83

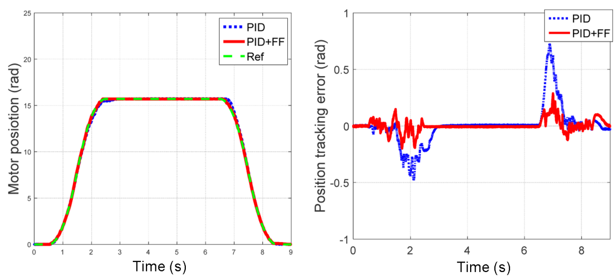

Figure 17. Experimental result of position tracking control with PID, PID+FF controller (middle load).

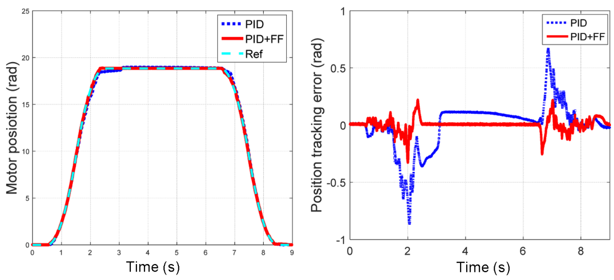

Figure 18. Experimental result of position tracking control with PID, PID+FF controller (high load).

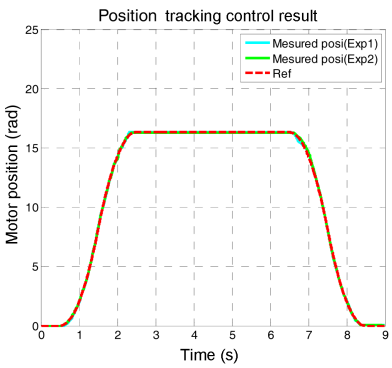

Figure 19. Position tracking control result with identified model and PID controller.

radian and 0.38 radian, respectively. Meanwhile, the model with the feed-forward controller had a maximum error and rms error of 0.32 radian and 0.13 radian, respectively.

The second method validated the model by observing the disturbance with a PID controller, feed-forward controller, and DOB. Figure 19 presents the position tracking control results with the second method. Two experimental results were shown to verify the reproducibility. Figures 20 and 21 show the observed even disturbance and odd disturbance, respectively. The dotted line represents the identified mode, and the solid line is the

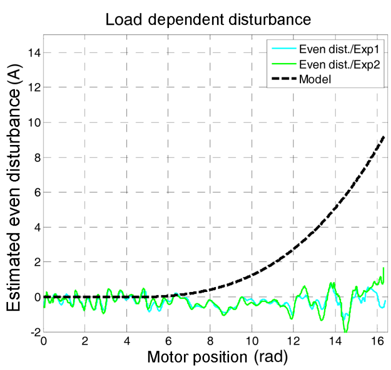

Figure 20. Observed load dependent odd disturbance with identified model and PID controller.

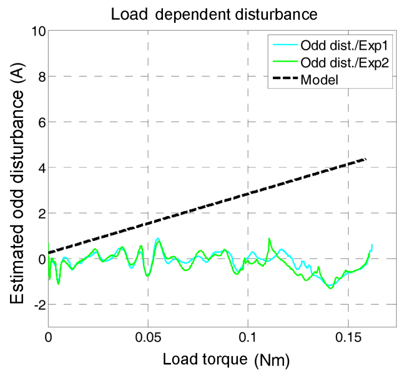

Figure 21. Observed load dependent even disturbance with identified model and PID controller.

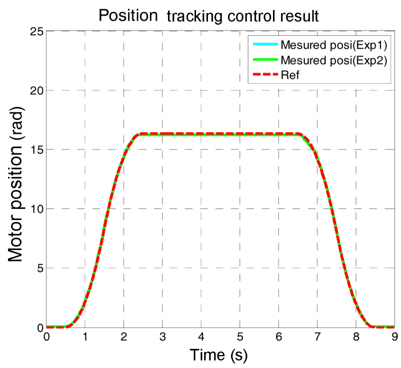

Figure 22. Position tracking control result with identified model and PD controller.

results of observation in the second experiment. Because the observed disturbance has values close to 0, we can presume that the identified model is similar to the actual plant.

Figures 22 and 23 are the results of experiments performed only with a PD controller and the model. Offset errors occur in the steady state as the friction model is less precise at low speeds. However, the identified model has a control precision of 0.1 rad, which is smaller than the

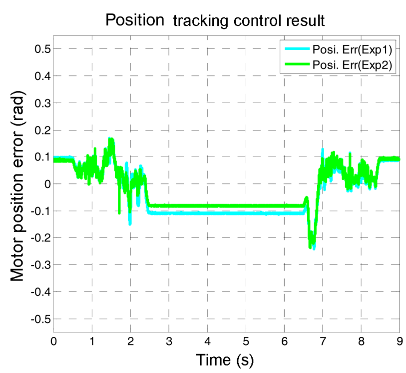

Figure 23. Motor position tracking error with identified model and PD controller.

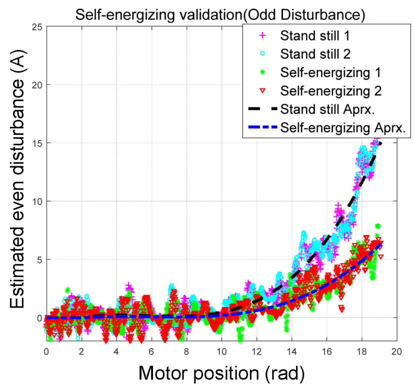

Figure 24. Self-energizing effect validation (even disturbance).

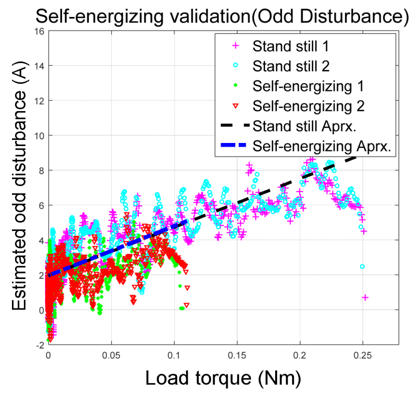

Figure 25. Self-energizing effect validation (odd disturbance).

required value of 0.5 rad, and thus can be considered acceptable.

5. ENGB SYSTEM SELF-ENERGIZING EFFECT VALIDATION

The proposed identification method can be used to validate the self-energizing effect of the ENGB system or EWB system. The existing method of validating the self-energizing effect in the EWB system compares the input and output in a steady state. The problem is that the frictional force in the stationary state changes according to transient conditions, and accurate validation is difficult because friction between the brake pad and disk is combined with friction due to the mechanical part. By separating the load and the friction of the mechanical part, the method proposed in this study can be applied to validate the self-energizing effect purely due to friction between the brake pad and disk.

Figures 24 and 25 show the disturbance observed when the self-energizing effect is produced, that is, situations in which the brake disk is motionless or rotating. The cross-shaped dots and circular dots represent the data obtained from the standstill situation, and the star-shaped dots and the triangular dots represent the data obtained from the rotating situation. The data obtained were in the form of a constant multiplied to the same-shaped model. The self-energizing effect is validated using only the even disturbance, which corresponds to the load, instead of the odd disturbance, which corresponds to the friction of the mechanical part. P in Equations (43) and (44) represents the self-energizing gain. Based on the model obtained while the brake disk is in a stationary state, a P value of 0.421 was derived from data for the rotating disk. This value was then substituted in Equation (43) to calculate the coefficient of friction of the brake pad. The coefficient of friction obtained through the experiment was 0.249.

$$f(x) = p(c_3x^3 + c_2x^2 + c_1x + c_0) \tag{43}$$

$$p = \frac{F_{\text{N,self-energizing}}}{F_{\text{N,w/o self-energizing}}} = \frac{(d/r)}{(d/r) - \mu} \tag{44}$$

6. CONCLUSION

This study performed model identification of the ENGB system using a DOB-based model identification method. By employing the nearest neighbor search method, the even-odd disturbance was separated without the influence of hysteresis even in situations with low control precision. The accuracy of the resulting ENGB system model was validated through experiments. The self-energizing effect due to friction between the brake disc and pad within the mechanical system was also validated.

REFERENCES

Balogh, L., Streli, T., Nemeth, H. and Palkovics, L. (2007). Modelling and simulating of self-energizing brake system. *Int. J. Vehicle Mechanics and Mobility* **44**, **1**, 368–377.

Fox, J., Roberts, R., Baier-Welt, C., Ho, L. M., Lacraru, L. and Gombert, B. (2007). Modeling and control of a single motor electronic wedge brake. *SAE Paper No*. 2007-01-0866.

Hartmann, H., Schautt, M., Pascucci, A. and Gombert, B. (2002). eBrake® - The mechatronic wedge brake. *SAE Paper No*. 2002-01-2582.

Ho, L. M., Roberts, R., Hartmann, H. and Gombert, B. (2006). The electronic wedge brake - EWB. *SAE Paper No*. 2006-01-3196.

Kim, S., Choi, S. and Kim, J. (2008). The design of electronic noncircular gear brake and adaptation scheme for pad friction-coefficient estimation. *KSAE Annual Conf. Proc., Korean Society of Automotive Engineers*, 1793–1801.

Kim, M., Jung, J., Chun, J. and Kim, J. (2009a). Control of an electromechanical brake for hybrid brake system. *KSAE Annual Conf. Proc., Korean Society of Automotive*

Engineers, 1445−1450.

Kim, J. G., Kim, M. J., Kim, J. K. and Noh, K. H. (2009b). Developing of electronic wedge brake with cross wedge. *SAE Paper No*. 2009-01-0856.

Roberts, R., Schautt, M., Hartmann, H. and Gombert, B. (2003). Modelling and validation of the mechatronic wedge brake. *SAE Paper No*. 2003-01-3331.

Roberts, R., Gombert, B., Hartmann, H., Lange, D. and Schautt, M. (2004). Testing the mechatronic wedge brake. *SAE Paper No*. 2004-01-2766.

Saric, S., Bab-Hadiashar, A. and Hoseinnezhad, R. (2008). Clamp-force estimation for a brake-by-wire system: A sensor-fusion approach. *IEEE Tans. Vehicular Technology* **57**, **2**, 778−786.

Schwarz, R., Isermann, R., Böhm, J., Nell, J. and Rieth, P. (1999). Clamping force estimation for a brake-by-wire actuator. *SAE Paper No*. 1999-01-0482.

Semsey, Á. and Roberts, R. (2006). Simulation and development of electronic wedge brake. *SAE Paper No*. 2006-01-0298.

Xiang, W., Richardson, P. C., Zhao, C. and Mohammad, S. (2008). Automobile brake-by-wire control system design and analysis. *IEEE Trans. Vehicular Technology* **57**, **1**, 138−145.